Comparative analysis of resonant phonon THz quantum cascade lasers

Christian Jirauschek,[a)] Giuseppe Scarpa, and Paolo Lugli
Institute for Nanoelectronics, TU München, Arcisstraße 21, D-80333 München, Germany

Miriam S. Vitiello and Gaetano Scamarcio
*CNR-INFM Regional Laboratory LIT^3 and Dipartimento Interateneo di Fisica "M. Merlin,"
Università degli Studi di Bari, Via Amendola 173, 70126 Bari, Italy*

We present a comparative analysis of a set of GaAs-based THz quantum cascade lasers, based on longitudinal-optical phonon scattering depopulation, by using an ensemble Monte Carlo simulation, including both carrier-carrier and carrier-phonon scattering. The simulation shows that the parasitic injection into the states below the upper laser level limits the injection efficiency and thus the device performance at the lasing threshold. Additional detrimental effects playing an important role are identified. The simulation results are in reasonable agreement with the experimental findings. © *2007 American Institute of Physics*. [DOI: 10.1063/1.2719683]

Quantum cascade lasers (QCLs) have an enormous potential as compact and efficient THz sources, promising mW level output power. Recently a scheme based on longitudinal-optical (LO) phonon scattering depopulation has been successfully demonstrated,[1–4] designed for high operating temperatures and reaching up to 164 K in pulsed and 117 K in continuous wave (cw) operation.[4] In these structures, the collector state is separated from the next lower level by at least the LO phonon energy, enabling efficient depletion of the lower radiative state by LO phonon scattering and reducing thermal backfilling. This overcomes the limitations associated with the conventional bound-to-continuum and chirped superlattice designs, where thermal backfilling of the lower radiative state prevents high temperature performance.

In this letter, we theoretically investigate three GaAs/Al$_{0.15}$Ga$_{0.85}$As THz QCL structures based on the above scheme and fabricated with high-confinement low-loss double metal waveguides. An experimental comparison between these structures was already carried out,[3] and motivates our theoretical comparative investigation. For the analysis, an ensemble Monte Carlo (MC) method is used,[5–7] which has successfully been applied to the theoretical investigation of such structures.[8–10] The subband energies and wave functions of the structure are calculated with a Schrödinger-Poisson solver, coupled to the MC simulation. The essential scattering mechanisms due to electron-electron, electron-LO phonon, and electron-acoustic phonon interactions are considered as described in Ref 6. Intercarrier scattering is implemented based on the Born approximation,[11,12] also taking into account the screening effects.[13] In the simulated structures, intercarrier scattering plays a major role for the intrasubband dynamics, while carrier transport is governed by LO phonon scattering for the temperature and doping level considered. Nonequilibrium phonon distributions are explicitly taken into account, and the Pauli's exclusion principle is also included. Due to the relatively low electron densities, the influence of such mechanisms is negligible.

Periodic boundary conditions are used, i.e., electrons coming out from one side of the device are automatically injected into the equivalent level on the opposite side.[7]

Figure 1(a) shows one period of the conduction band structure of the 2.8 THz QCL[3] calculated at 11.3 kV/cm; the band profiles of the other structures discussed here are similar. The upper and lower levels of the lasing transition around 2.8 THz are labeled 5 and 4, respectively. Efficient depopulation of level 4 is achieved via the collector state 3, which is in turn separated from the levels 2 and 1 by roughly the optical phonon energy (36 meV), thus enabling efficient depletion to these levels by optical phonon scattering. Parasitic channels counteracting the onset of population inversion between levels 5 and 4 are provided by the injection from levels 1′ and 2′ (i.e., the replica of levels 1 and 2 situated in the adjacent period on the right side of Fig. 1) into levels 1 −4, and by scattering processes from the upper laser level to the states below. In Fig. 1(b), the level energies of the 2.8 THz design are shown as a function of the applied electric
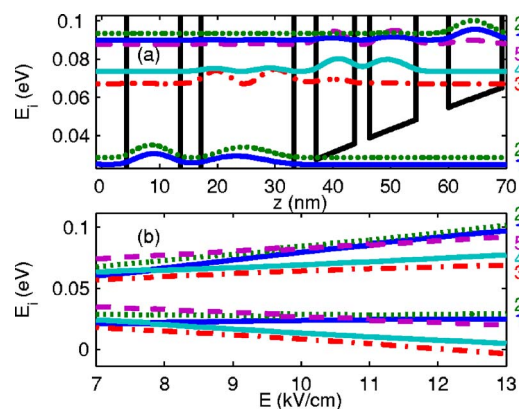

FIG. 1. (Color online) (a) Conduction band profile and probability densities of a 2.8 THz QCL based on a phonon depopulation scheme at 11.3 kV/cm. The layer thicknesses of one period, starting from the injection barrier, are 56/93/36/160/39/67/25/81 [Å]. The underlined layer is doped at $N=1.9 \times 10^{16}$ cm^{-3} and the sheet density for one period is $n_{2D}=3\times10^{10}$ cm^{-2}. (b) Level energies as a function of the applied field for two periods of the 2.8 THz structure.
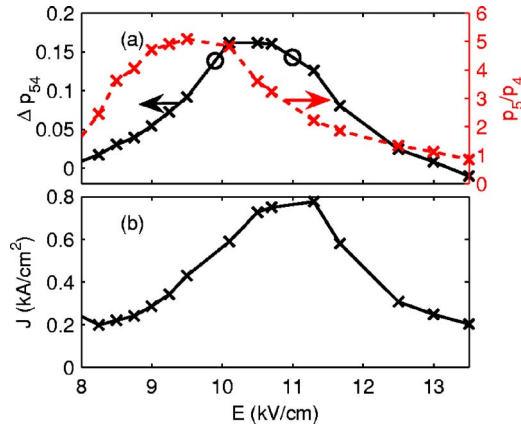
a)Electronic mail: jirauschek@tum.de

FIG. 2. (Color online) Simulation results for the 2.8 THz structure as a function of the applied field (E). The crosses mark the sampling points; the lines are guide to the eye. (a) Relative population difference (solid line) and inversion (dashed line) between the upper and lower laser level. The circles mark the positions of the anticrossings $5-2'$ and $5-1'$. (b) Current density, plotted as a function of E.
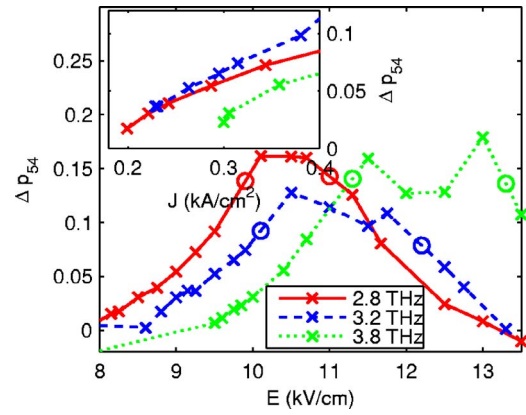

FIG. 3. (Color online) Population difference between upper and lower laser level as a function of the applied field. The circles mark the positions of the anticrossings $5-2'$ and $5-1'$. The inset shows Δp_{54} as a function of the current density close to the onset of inversion. The crosses mark the sampling points; the lines are guide to the eye.

field. The strong anticrossings between level 5 and the injection levels $2'$ and $1'$ around 9.9 and 11 kV/cm facilitate a selective injection into the upper laser level, leading to a reduction of the parasitic channels. Around 7.6 kV/cm, there is an additional anticrossing between levels $1'$ and 4, causing a strong parasitic injection into the lower laser level.[8] The energy difference between the collector state 3 and the injector state 2 (1) increases from 28 meV (36 meV) for 7 kV/cm to 40 meV (44 meV) for 13 kV/cm, enabling an efficient LO-phonon-induced depletion of the lower laser level especially for biases >10 kV/cm.

Figure 2 shows MC simulation results for the 2.8 THz structure at a lattice temperature of 100 K. The sampling electric fields were chosen as to avoid the excessive current spikes emerging near narrow anticrossings in MC simulations.[8] It should be pointed out that sharp anticrossing features are an artifact of the Schrödinger solution in the absence of broadening mechanisms (such as those provided by surface roughness). If a more precise quantum mechanical approach were used based, for example, on density matrices[14–16] or nonequilibrium Green's funcions,[17] much smoother features would be observed, that would nevertheless not drastically modify our analysis. In Fig. 2(a), the difference and ratio of the relative population in the upper (p_5) and lower (p_4) laser levels is displayed, with $\Delta p_{54} = p_5 - p_4$. The current density in Fig. 2(b) exhibits a parasitic peak (not shown) around the $1'-4$ anticrossing and a local minimum at 8.25 kV/cm. It reaches its maximum around the two anticrossings of level 5 with the injector states $1'$ and $2'$, where the injection into subband 5 is most efficient. In addition, the energy difference between the collector state 3 and levels 2,1 is designed to reach the LO phonon energy in this bias range and thus become favorable for LO phonon-induced depletion of level 4. These two effects combine to yield a large population difference of Δp_{54} and thus a high material gain between 10 and 11 kV/cm.

The calculated inversion peak $p_5/p_4 = 5.1$ lies above the experimentally measured maximum $p_5/p_4 = 2.58 \pm 0.52$,[3] and also the experimentally measured current density peak[3] is

overestimated by about 40%. This is a well-known phenomenon for MC simulations of structures dominated by LO phonon-induced carrier transport,[8,18] and may partly be due to the absence of broadening mechanisms in the algorithm, as discussed above. To some extent, the deviation can also be ascribed to a lower than specified free-carrier density in the sample. In addition, the experimental effective current density, which has been calculated based on an effective area, is smaller than the on-axis value in the gain medium. The simulated inversion peak is shifted by -2.4 kV/cm relative to the experimental maximum, which occurs at 11.9 kV/cm,[19] and the current density peak is shifted by a similar amount. Possible explanations are an additional parasitic resistance in the experimental structure or deviations in the growth process.

In Fig. 3, the population difference Δp_{54} is plotted as a function of the electrical field for three THz QCLs operating at 2.8 THz,[3] 3.2 THz,[2] and 3.8 THz.[1] The maximum of Δp_{54} in Fig. 3, which occurs at an especially high bias for the 3.8 THz structure in agreement with the experiment,[1] is for all designs located around the two anticrossings of level 5 with the injector states. The inset shows Δp_{54} close to the onset of inversion as a function of the current density, for values ranging between the minimum value after the parasitic $1'-4$ anticrossing peak and 0.4 kA/cm². This corresponds to an electrical field range of $8.25-9.4$, $9.15-10.4$, and $9.85-10.5$ kV/cm for the 2.8, 3.2, and 3.8 THz design, respectively. In the 2.8 and 3.2 THz structures, the onset of inversion occurs at much smaller current densities than for the 3.8 THz one, which is an indication of the weaker parasitic channel $1'-4$. These findings are in agreement with the experimental results, which yield a significantly reduced threshold current for the 2.8 and 3.2 THz structures as compared to the 3.8 THz design.[3]

To further investigate the structures, we introduce the injection efficiency $\eta_{inj,i}$ from a given period into a level i of the next-lower period, defined as the ratio between the carriers injected into level i and the total amount of carriers injected into that period. An overview of the simulation results is given in Table I. The low inversion in the 3.8 THz structure at $J = 0.3$ kA/cm² can be partly attributed to the

TABLE I. Overview over simulation results for the 2.8/3.2/3.8 THz structure close to the onset of inversion.

Quantity	$J = 0.3$ kA/cm^2	$J = 0.4$ kA/cm^2
$p_5 (\%)$	7.5/8.2/3.5	10.6/13.8/7.9
$p_4 (\%)$	1.6/1.5/1.2	2.1/2.5/1.3
$\eta_{\text{inj},5} (\%)$	43.3/42.8/26.1	42.9/48.4/40.1
$\eta_{\text{inj},4} (\%)$	14.6/15.2/22.6	16.3/18.9/13.6
$\eta_{\text{inj},3} (\%)$	20.9/23.6/17.8	23.0/21.9/26.1
$\eta_{\text{inj},2} (\%)$	3.5/3.2/12.2	3.4/2.2/9.3
$\eta_{\text{inj},1} (\%)$	14.2/10.7/19.2	13.0/7.7/9.9
$\tau_5 (\text{ps})$	2.75/3.05/2.02	2.96/3.43/2.18
$\tau_{5\rightarrow 4} (\text{ps})$	11.1/11.7/13.7	10.1/9.7/11.9
$\tau_4 (\text{ps})$	0.97/0.88/0.68	0.88/0.83/0.71
f_{54}	0.65/0.53/0.78	0.52/0.49/0.72

poor injection efficiency into the upper laser level $\eta_{\text{inj},5}$, which is only 26% for the 3.8 THz design, as compared to over 40% for the other structures. This is due to the strong parasitic injection into the states below the upper laser level, as indicated by the increased $\eta_{\text{inj},1,\dots,4}$. From Table I we can see that also for the 2.8 and 3.2 THz designs, the parasitic injection channels to levels $1-4$ play a significant role in the threshold region. To obtain a high inversion, long lifetimes τ_5 and $\tau_{5\rightarrow 4}$ are desirable,[20] as well as a small τ_4 ensuring a fast depopulation of the lower laser level. Furthermore, the gain is directly proportional to the reduced oscillator strength f_{54}.[8] τ_5 in the 3.8 THz structure is reduced mainly due to an increased leakage to levels 3 and 1, while the values of τ_4 and f_{54} are slightly superior for this design. At low current densities, the 2.8 THz structure shows a higher value of f_{54} than the 3.2 THz laser, outweighing the somewhat lower inversion and resulting in a slightly better threshold performance, as experimentally observed.[3]

We have also calculated the electron-lattice energy relaxation rate τ_E^{-1}.[21] Such a quantity reaches its peak in the lasing region, where the phonon-assisted injection into the upper laser level and depletion of the lower laser level are the strongest. For the best of the structures (2.8 THz), a maximum τ_E^{-1} of approximately 3.8 ps^{-1} was calculated, in reasonable agreement with the experiment.[3] The other two structures show a lower maximum value of τ_E^{-1} (3.3 ps^{-1}), also in qualitative agreement with the experiment. For some of the subbands, the simulation yields highly nonequilibrium carrier distributions, complicating the comparison with experimentally extracted temperatures.[3] However, an investiga-

tion of this issue goes beyond the framework of this paper and will be addressed in a different article.

In conclusion, we have shown that the MC simulation allows us to identify the parasitic processes affecting the operation of THz lasers, thus providing a meaningful explanation of the experimental findings.

[1] B. S. Williams, S. Kumar, H. Callebaut, Q. Hu, and J. L. Reno, Appl. Phys. Lett. **83**, 5142 (2003).
[2] S. Kumar, B. S. Williams, S. Kohen, Q. Hu, and J. L. Reno, Appl. Phys. Lett. **84**, 2494 (2004).
[3] M. S. Vitiello, G. Scamarcio, V. Spagnolo, B. S. Williams, S. Kumar, Q. Hu, and J. L. Reno, Appl. Phys. Lett. **86**, 111115 (2005).
[4] B. S. Williams, S. Kumar, Q. Hu, and J. L. Reno, Opt. Express **13**, 3331 (2005).
[5] F. Compagnone, A. Di Carlo, and P. Lugli, Appl. Phys. Lett. **80**, 920 (2002).
[6] M. Manenti, F. Compagnone, A. Di Carlo, P. Lugli, G. Scamarcio, and F. Rizzi, Appl. Phys. Lett. **82**, 4029 (2003).
[7] R. C. Iotti and F. Rossi, Appl. Phys. Lett. **78**, 2902 (2001).
[8] H. Callebaut, S. Kumar, B. S. Williams, Q. Hu, and J. L. Reno, Appl. Phys. Lett. **83**, 207 (2003).
[9] H. Callebaut, S. Kumar, B. S. Williams, Q. Hu, and J. L. Reno, Appl. Phys. Lett. **84**, 645 (2004).
[10] O. Bonno, J.-L. Thobel, and F. Dessenne, J. Appl. Phys. **97**, 043702 (2005).
[11] S. M. Goodnick and P. Lugli, Phys. Rev. B **37**, 2578 (1988).
[12] M. Moško, A. Mošková, and V. Cambel, Phys. Rev. B **51**, 16860 (1995).
[13] S. M. Goodnick and P. Lugli, Appl. Phys. Lett. **51**, 584 (1987).
[14] R. C. Iotti and F. Rossi, Phys. Rev. Lett. **87**, 146603 (2001).
[15] H. Callebaut and Q. Hu, J. Appl. Phys. **98**, 104505 (2005).
[16] C. Weber, F. Banit, S. Butscher, A. Knorr, and A. Wacker, Appl. Phys. Lett. **89**, 091112 (2006).
[17] S.-C. Lee, F. Banit, M. Woerner, and A. Wacker, Phys. Rev. B **73**, 245320 (2006).
[18] R. Köhler, A. Tredicucci, F. Beltram, H. E. Beere, E. H. Linfield, A. G. Davies, D. A. Ritchie, R. C. Iotti, and F. Rossi, Nature **417**, 156 (2002).
[19] The experimental electric field values were computed from the measured voltages subtracting the voltage drop at the top Schottky barrier and dividing the resultant bias by the active region thickness, assuming a constant field in the gain medium.
[20] τ_5 and $\tau_{5\rightarrow 4}$ are defined as the characteristic times for relaxation from level 5 to all lower levels and to level 4 alone, respectively, and already include the effect of backscattering from the final state (Ref. 8).
[21] τ_E is here calculated as $\tau_E = (E_{\text{kin},e} - E_{\text{kin},e}^{\text{eq}})/P_{\text{th}}$, where $E_{\text{kin},e}$ is the total kinetic energy of the N simulated electrons and $E_{\text{kin},e}^{\text{eq}} = N k_B T_L$ is the equilibrium kinetic energy at lattice temperature T_L. The dissipated thermal power P_{th} is computed as the product of the calculated current and the applied voltage.